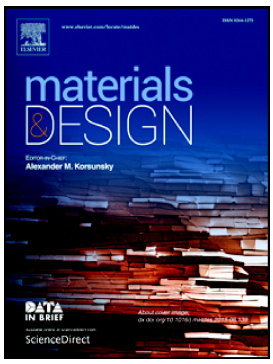

Dynamic response and energy absorption of functionally graded porous structures

Da Chen, Sritawat Kitipornchai, Jie Yang

PII: S0264-1275(17)31124-3
DOI: doi:10.1016/j.matdes.2017.12.019
Reference: JMADE 3570

To appear in: *Materials & Design*

Received date: 23 June 2017
Revised date: 6 December 2017
Accepted date: 10 December 2017

Please cite this article as: Da Chen, Sritawat Kitipornchai, Jie Yang , Dynamic response and energy absorption of functionally graded porous structures. The address for the corresponding author was captured as affiliation for all authors. Please check if appropriate. Jmade(2017), doi:10.1016/j.matdes.2017.12.019

Dynamic response and energy absorption of functionally graded porous structures

Da Chen [a], Sritawat Kitipornchai [a], Jie Yang [b,*]

[a] *School of Civil Engineering, the University of Queensland, Brisbane, St Lucia, QLD 4072, Australia*

[b] *School of Engineering, RMIT University, PO Box 71, Bundoora, VIC 3083 Australia*

[*]Corresponding author.

E-mail address: j.yang@rmit.edu.au (J. Yang).

Abstract

This paper is focused on the in-plane crushing of two-dimensional (2D) porous structures with a special attention on the effect of functionally graded (FG) porosities. The dynamic response and energy absorption of closed-cell metal foams with different porosity distributions are investigated by using finite element (FE) analysis. Two symmetric, two asymmetric and one uniform distributions of internal pores along the impact direction are constructed with Voronoi tessellation. The proposed porous structure is crushed under the impact of a rigid panel with a constant velocity. The deformation of cell walls is simulated using a plastic kinematic material model. The erosion criteria and hourglass control are applied to ensure the accuracy of numerical results, which are validated against the experimental data from open literature. The effects of varying parameters on the energy absorption, deformation pattern, and stress-strain curve of the FG porous structure are discussed. The dynamic response is found to be influenced by different random cell geometries, porosity gradients, cell wall thicknesses, internal pore numbers, and impact velocities. The effective way to improve energy absorption capability of the porous structure under a constant-velocity impact is proposed, shedding new insights into the deformation mechanism of the FG porous structure for engineering design.

Keywords:

Functionally graded porous structures, dynamic response, energy absorption, Voronoi tessellation, finite element analysis.

1. Introduction

Metal foams have been widely used in various engineering applications, including sandwich panels, acoustic dampers, heat diffusers, electrodes and batteries [1-11], due to their excellent mechanical, thermal and electrical properties. Originated from the novel deformation behavior of internal cells, the superior dynamic performance and energy absorption capacities of porous structures, especially metal foams, also make them promising candidates for structural protection against impact, blast and explosion. Although extensive researches have been conducted is this area [12-18], the effective method to improve the energy absorption of porous structures hasn't been well studied either theoretically or experimentally.

Many studies have been reported on the effects of porosity geometry, crushing stress and strain, and deformation behavior of porous structures to characterize the dynamic response and energy absorption. Zheng at al. [19] investigated the dynamic impact behaviour of metal foams by using a three-dimensional (3D) FE model under different loading conditions and rates. Kader et al. [20] presented an FE analysis based on a mesoscale approach and plate-impact experiments to investigate the elastic-plastic behavior of core collapse. Li et al. [21] built a 2D random cellular solid model to characterize Poisson's ratio and energy absorption of porous structures with varying relative densities and area compression ratios. Fang et al. [22] constructed a 3D mesoscopic model of closed-cell aluminium foams and conducted numerical simulations for energy absorption capability. Vesenjak et al. [23] carried out FE and experimental analyses of open-cell metal foams with a special focus on the anisotropy and strain rate sensitivity.

Compared with conventional porous structures, FG porous structures with graded porosity distributions possess advantageous mechanical properties. Numerous studies have been conducted on their static and dynamic performance. Chen et al. [24-26] gave a detailed

research concerning the elastic buckling, static bending, free and forced vibrations of porous beams with different FG porosity distributions. Kitipornchai et al. [27, 28] presented linear and nonlinear studies on the buckling and vibration behaviours of nanocomposite beams reinforced by graphene platelets, and focused on the influence of non-uniform porosities. Magnucka-Blandzi [29] carried out a dynamic stability analysis on a radial compressed metal foam circular plate and discussed the effect of porosity on critical loads. Mojahedin et al. [30] investigated the buckling behavior of FG circular plates made of saturated porous materials and employed the higher order shear deformation plate theory to derive the governing equations. It has been found from the above studies that an appropriately selected FG porosity distribution does improve the structural stiffness of porous beams and plates at a certain level. Thus, it is highly possible that FG porosity can be an effective way to improve the energy absorption capacity as well.

However, the dynamic response and energy absorption of FG porous structures under impact loading, though important, still haven't been studied systematically. Currently, only very limited researches were conducted in this area. Koohbor and Kidane [18] proposed a design optimization for continuously and discretely graded polymeric foams, and presented the effect of density gradation on the load bearing and energy absorption. Ajdari et al. [31] developed FE models to analyse the crushing behavior and energy absorption of regular, irregular and FG cellular structures, including 2D honeycombs with both regular hexagonal and irregular distributions. Liang et al. [32] carried out a theoretical and numerical investigation on the blast responses of one-dimensional continuous-density graded porous bars based on the rigid-perfectly plastic-locking model and FE analysis.

This paper presents a numerical simulation of in-plane crushing of 2D FG porous structures made of closed-cell metal foams under constant-velocity impacting. Voronoi tessellation and FE modelling are briefly introduced. The present analysis is validated against

the experimental data in a split Hopkinson pressure bar test from open literature. The dynamic responses of porous structures with uniform and non-uniform porosity distributions are compared. Varying random cell geometries, porosity gradients, cell wall thicknesses, internal pores numbers, and impact velocities show different influences on the energy absorption, deformation pattern, and stress-strain curve. The proposed design of non-uniformly asymmetric distribution of internal pores can effectively improve the energy absorption capacity of porous structures under a higher-velocity impact.

2. Numerical modelling

2.1. Porosity distributions

Five different porosity distributions are considered in this paper, as illustrated in Figs. 1A-1E, in which distributions A and B are non-uniformly symmetric, distributions C and D are non-uniformly asymmetric, and distribution E denotes the uniform porosity. The proposed 2D porosities are constructed in an area of 0.05 m × 0.05 m based on Voronoi tessellation. The cell wall thickness is assumed to be 0.1 mm, unless stated otherwise.

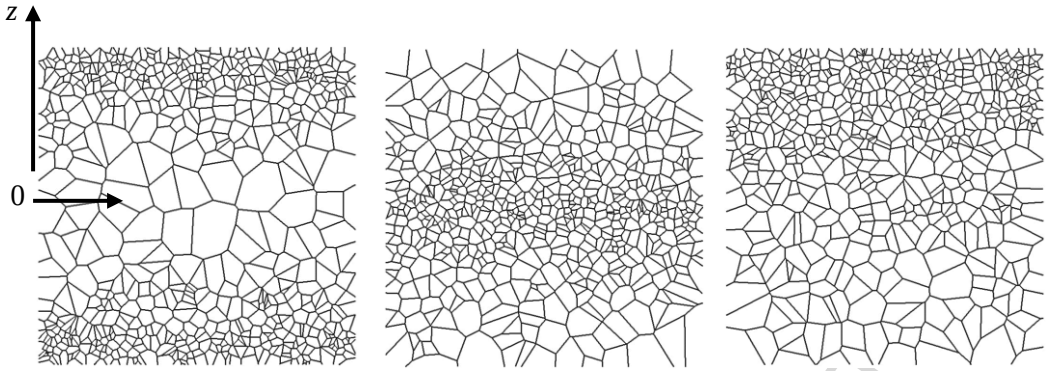

(A) Distribution A (symmetric I)

(B) Distribution B (symmetric II)

(C) Distribution C (asymmetric I)

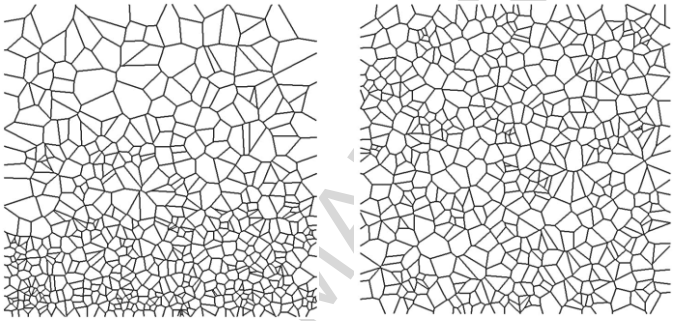

(D) Distribution D (asymmetric II)

(E) Distribution E (uniform)

Fig. 1. Porosity distributions.

The number of internal pores for non-uniform distributions varies smoothly along the thickness. Based on the coordinate system given in Fig. 1 (A), where *z*-axis is along the thickness direction and the origin point is on the mid-plane, the variation of internal pore number $\mathrm{S}(z)$ for distributions A-D can be approached by using polynomial curve fitting with a three-order polynomial as

$$\mathrm{S}(z) = \mathrm{S}_1 z^3 + \mathrm{S}_2 z^2 + \mathrm{S}_3 z + \mathrm{S}_4 \tag{1}$$

of which the coefficients S_1, S_2, S_3 and S_4 are listed in Table 1. For symmetric distributions A and B, $S(z)$ denotes the internal pore number when $0 < z < 0.025\,\mathrm{m}$, while that of asymmetric distributions C and D corresponds to the whole domain with $-0.025\,\mathrm{m} < z < 0.025\,\mathrm{m}$.

Table 1

Coefficient in polynomials of internal pore numbers for different porosity distributions.

Porosity distribution	S_1	S_2	S_3	S_4	z (m)
Distribution A	-2.9447e6	1.4895e5	-301.3133	11.2830	$0 < z < 0.025$
Distribution B	-1.6837e3	2.2661e4	-2.1748e3	51.3918	$0 < z < 0.025$
Distribution C	1.5015e5	8.6806e3	638.3266	25.5700	$-0.025 < z < 0.025$
Distribution D	-1.5015e5	8.6806e3	-638.3266	25.5700	$-0.025 < z < 0.025$

The relative density of porosity distributions is calculated by

$$\text{Relative density} = \frac{\text{Structural area}}{0.05\,\mathrm{m} \times 0.05\,\mathrm{m}} \tag{2}$$

All the porosity distributions in Fig. 1 have similar relative densities with difference less than 1.0 %, as tabulated in Table 2. Please note that although the overall distributions of internal pores are described as either graded or uniform, the randomness of porosity geometry is considered to simulate metal foams in reality.

Table 2

Relative density of different porosity distributions in Fig. 1.

Porosity distribution	Relative density (%)
Distribution A	9.0311
Distribution B	9.0211
Distribution C	9.0077
Distribution D	9.0077
Distribution E	8.9796

2.2 Voronoi tessellation

The outstanding issues in computational modelling of metal foams are mainly focused on how to model the internal pores, which are usually randomly shaped and located. The original diversity of porosity geometries makes it very difficult for current researches to give reliable predictions of metal foams. Those based on the scanning electron microscope (SEM) imaging are only modelling specific types of metal foams. This paper applies Voronoi tessellation to generate the porosity geometry, which is an effective way to construct the closed-cell porosities and considers the randomness of pore shapes and locations simultaneously. It is commonly used in relevant studies. Given a set of initial points p_1, p_2, $\cdots$, p_n, a typical 2D Voronoi diagram divides the plane into *n* regions by drawing the perpendicular bisectors of line segments $\overline{p_i p_j}$ $(1 \le i(j) \le n,\ i \ne j)$, as shown in Fig. 2 [33], where each region denotes an internal pore. By dividing a square area (0.05 m × 0.05 m) into nine layers with identical thickness (0.05/9 m) and distributing different numbers of initial points in each layer, FG porosities can be constructed as depicted in Fig. 1 with Voronoi tessellation. The initial points

in each layer are randomly distributed, resulting in irregular size, shape, and location of internal pores. The foregoing algorithm is programmed in MATLAB and the geometry model is generated by using ANSYS/APDL, then imported into the numerical calculation code LS-DYNA for explicit dynamic analysis.

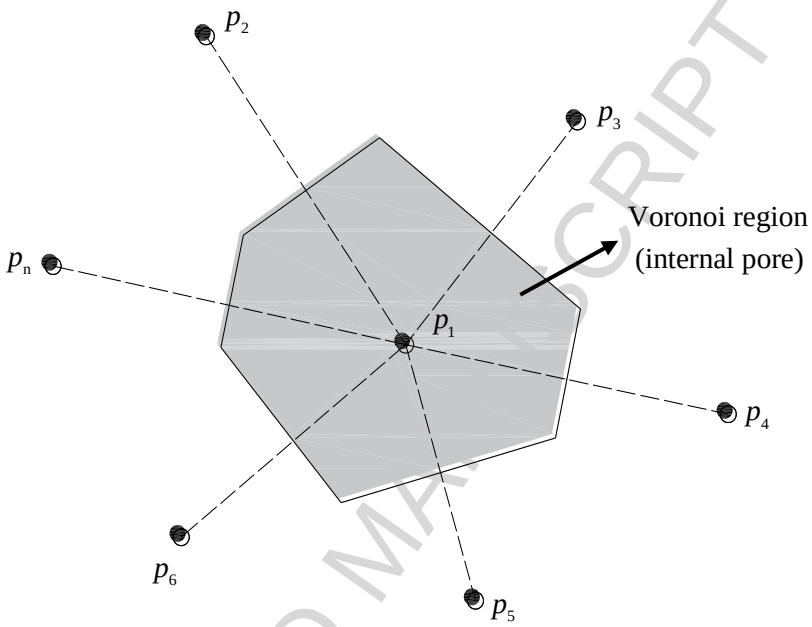

Fig. 2. Voronoi diagram.

2.3 Finite element analysis

In this study, an impact rigid panel is placed on the top of porous structures with a constant velocity V pointing downwards along the thickness direction, as illustrated in Fig. 3. Meanwhile, a stationary rigid panel is fixed on the bottom to support the structure, of which the top and bottom are labelled as the impact and stationary ends, respectively. During the crushing progress, the porous structure can deform freely in the plane. All the translational movements along the out-of-plane axis are constrained. For a single node in the porous structure, neither the translational constraints in the local horizontal and vertical directions

nor the rotational constraint about the local out-of-plane axis are applied. The impact panel can only move in the vertical direction.

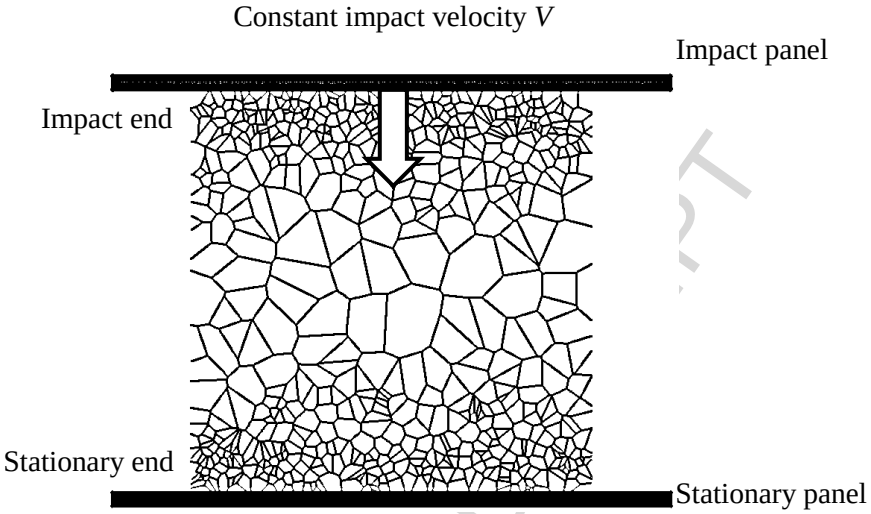

Fig. 3. Schematic diagram of the constant-velocity impacting.

LS-DYNA is employed to solve the equation of motion in FE analysis with Central Difference method for explicit time integration [34]. The deformation of cell walls is simulated by using the plastic kinematic material model with kinematic hardening plasticity, of which the typical elastic-plastic behavior is depicted in Fig. 4, where E is Young's modulus and E_t is Tangent modulus [35]. In this paper, the porous structures are assumed to be made of Al-Si-Mg alloy foams with the following material parameters: Young modulus $E = 70$ GPa, Tangent modulus $E_t = 4.62$ GPa, yield stress $\sigma = 185$ MPa, mass density $\rho = 2730$ kg/m^3, Poisson's ratio $\mu = 0.34$ [22]. This material model is assumed to be strain rate insensitive, as no air flow is considered in this study and this rate effect is insignificant for low-density aluminium foams [22, 36-39]. The automatic single surface contact is applied on the cell surfaces, while the automatic surface to surface contact is employed to measure the mutual effects between the porous structure and rigid panels with the dynamic friction

coefficient as 0.15 [21], which is actually reported as an insensitive parameter by other studies [40, 41].

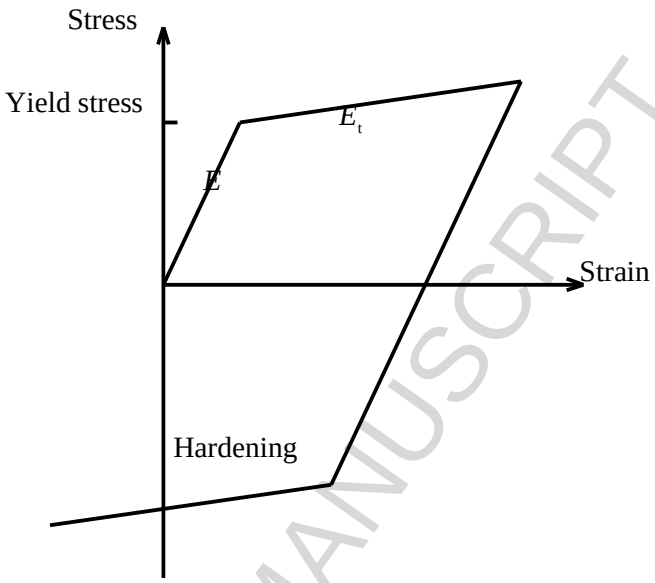

Fig. 4. Typical elastic-plastic behavior of the plastic kinematic material model [35].

The geometry model of porous structures is meshed by using the default Belytschko-Tsay shell element (5 degree of freedom in local coordinate system) with the characteristic length as 0.1 mm, which is determined based on a mesh sensitivity analysis given in section 3.2. The erosion criteria for cell walls are also applied with the maximum principal strain of 0.89 and shear strain of 0.96 [22]. Based on the first-order plate theory, the shear correction factor for shell elements is set as $5/6$. Hourglass (HG) control is important and needs to be included in the calculation as well [42]. HG-shaped elements are characterized with the non-physical zero energy mode, resulting in inaccurate stresses, strains, and deflections. To minimize the HG energy, this paper implements HG control with HG viscosity type IHQ = 4 (stiffness form of Flanagan-Belytschko integration) and HG coefficient QH = 0.05.

It should be noted that there are several significant weaknesses of 2D modellings in this matter. On one hand, 2D modelling can only be used for the closed-cell metal foams described in this paper. As for the open-cell metal foams, their cross sections involve unconnected cell walls, which are not possible to be reasonably simulated with 2D modelling. On the other hand, 2D modelling is only dealing with a single section of metal foams, of which the deformation is restricted in the plane only. The out-of-plane deformation is ignored completely, which is not the case in the reality. Thus, the obtained stress and strain fields with 2D modelling are always questionable to reflect the true response of 3D structures. Moreover, the results from 2D modelling are very difficult to be validated. Actually, most of the publications concerning the 2D modelling of porous structures cannot provide a validation analysis at all. This is due to the fact that the 2D modelling simply cannot capture the randomness of internal pores in all directions. The mentioned restricted deformation pattern contributes to this as well. Meanwhile, with 3D modelling, the open-cell metal foams, out-of-plane deformations, and the all-around randomness can be well simulated.

However, 2D modelling has its own unique advantages compared with the 3D modelling. First, the calculation efficiency of 2D modelling is much better than that of 3D modelling, which can easily cause unaffordable work load especially for dynamic crushing analysis. This is extremely important for studies dealing with multiple models like those in this paper.

Second, the 2D modelling excludes the effect of random porosities along the out-of-plane direction and presents more clear geometry design. Constructing various porosity distributions in 2D models can be more straight-forward to show how the internal pores vary along certain direction. While the 3D modelling has to consider the porosity variation in all directions, which may bring unnecessary influence to the results if the study is only about a specific porosity pattern.

Our study is focused on the closed-cell metal foams and the functionally graded porosities, which contain internal pores non-uniformly distributed only in one direction and can be sufficiently and clearly presented by using the 2D modelling. Different porosity distributions and impact velocities are considered here, resulting in a huge and unbearable work load if 3D modelling is adopted. Furthermore, 2D modelling can also provide reasonable predictions as shown in the following validation analysis. Therefore, employing 2D modelling in this study is appropriate considering the research propose and all the mentioned issues.

3. Numerical results

3.1 Validation study

The validation study is conducted to verify the validity of the presented geometry constructing and parameter setting. The stress-strain curves based on the impact contact force calculated from the model in Fig. 5 (A) are compared to those obtained in a split Hopkinson pressure bar test with a closed-cell aluminium foam [43]. The validation model has the same external size and similar relative density (26 mm × 26 mm and 10.2 %) as those of the experimental specimen (26 mm × 26 mm and 10 %). The cell wall thickness is assumed to be 0.09 mm. Fig. 5(B) and Fig. 5(C) present the comparisons of stress-strain curves under different strain rates. The values of external force F in the FE analysis are determined to obtain the strain rates similar to those in the experiment with $F = 35$ N and $F = 50$ N for 500 s^{-1} and 900 s^{-1} strain rates, respectively. It can be seen that our results agree well with the experimental data. The values of Pearson's linear correlation coefficient are 0.9073 and -0.1311 for the comparisons in Fig. 5(B) and Fig. 5(C), respectively, indicating a good correlation for the data in Fig. 5(B). Although those in Fig. 5(C) are poorly related, the values of stress are still close enough. Please note that during the FE analysis, the strain rate of

porous structure is generally growing due to the constant loading condition. The results under strain rates close to 500/900 s-1 are extracted for the comparisons.

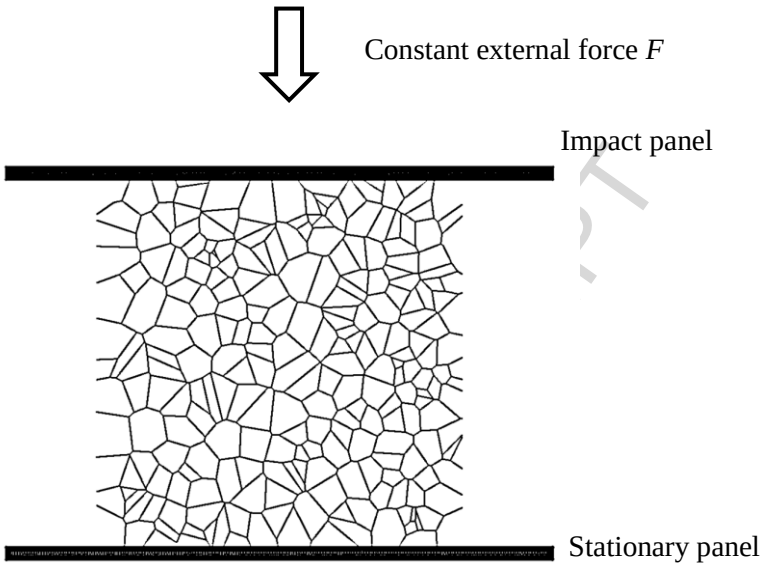

(A) Schematic diagram of the validation model.

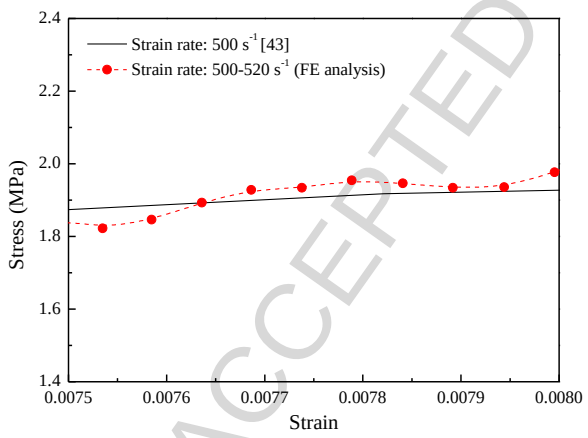

(B) Strain rate: 500 s^{-1}

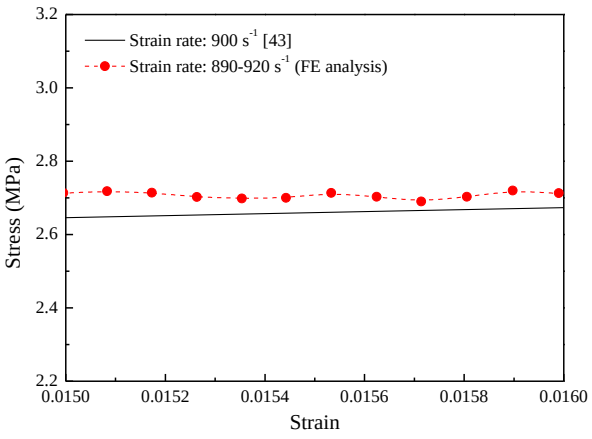

(C) Strain rate: 900 s^{-1}

Fig. 5. Validation model and comparison results.

It should be noted that most of the experimental studies on metal foams fail to give a detailed description of the specimens, such as the distribution pattern of internal pores and the cell wall thickness, which brings difficulties to the corresponding numerical modelling.

Especially for 2D modelling, if the internal pores of specimens change a lot in all direction, a big gap between the numerical and experimental results can be expected. However, this is actually quite reasonable due to the geometrical randomness. Thus, the best method is to build the models based on the SEM imaging or to manufacture the specimens with 3D printing to obtain the perfect match between the numerical models and metal foams used in experiments.

3.2 Mesh sensitivity analysis

A mesh sensitivity analysis concerning different porosities under varying impact velocities is conducted to determine the suitable element size employed in this study. Fig. 6(A) and Fig. 6(B) present the effects of element size on the energy absorptions of porous structures with distributions B and C under 100 m/s and 200 m/s impact velocities, respectively. The energy absorption is obtained based on the internal energy computed in the FE analysis, which is the total strain energy of all elements per volume. Please note that the stored elastic strain energy is included in the absorbed energy along with the dissipated plastic energy, since the elastic energy also contributes to the converting of input kinetic energy during the proposed crushing progress. It is observed that the results for 0.0001333 m and 0.0001 m are very close in both examples with difference less than 5 %. Therefore, 0.0001 m is employed as the element size in following calculations, which is illustrated in Fig. 6(C). Please notes that the nominal strain presented in this paper is up to 0.8, which is sufficient for this research and can be well simulated with the given finite element models. But for other studies arming to investigate the crushing response with higher strains, the settings and models need to be revised accordingly to achieve the reasonable accuracy of the results.

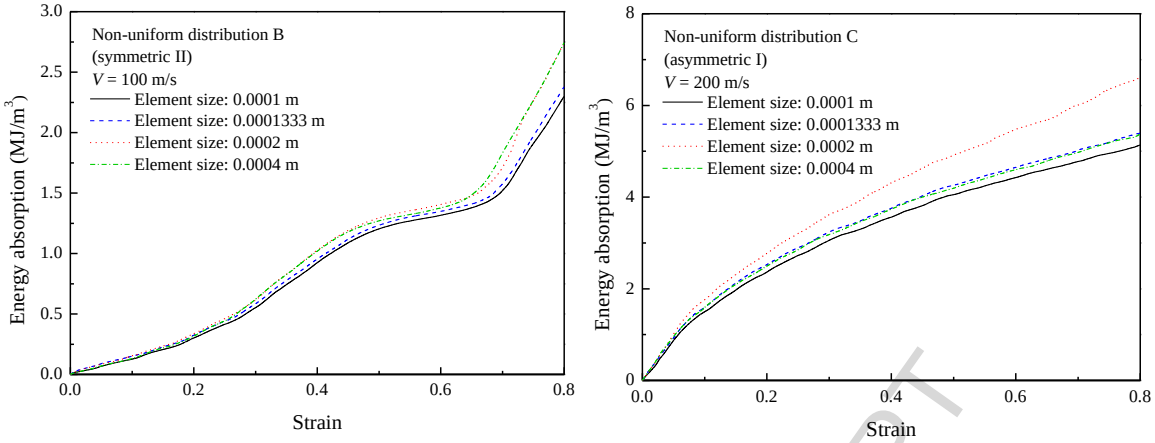

(A) Distribution B (100 m/s impact velocity) (B) Distribution C (200 m/s impact velocity)

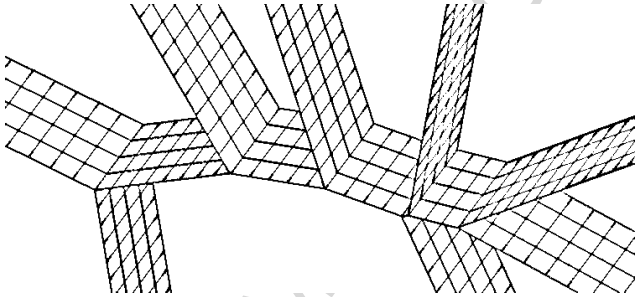

(C) Employed element size (0.0001 m)

Fig. 6. Mesh sensitivity comparisons and the employed element size.

3.3 Effect of random cell geometry

In sections 3.3-3.6, the effects of random cell geometry, porosity gradient, cell wall thickness, and internal pore number are examined by taking similar non-uniform symmetric distributions as typical examples. In the following section 3.7, the comparison between different porosity distributions under varying impact velocities is conducted based on the fixed porosity patterns shown in Fig. 1. The employed cell wall thickness for porosities in sections 3.3, 3.4, 3.6, and 3.7 is 0.1 mm.

The randomness of cell geometry involves random pore size, shape, and location. Three different random geometries for uniform symmetric porosity are constructed, as shown in Fig. 7, of which Randomness I in Fig. 7(A) is the same as the porosity distribution A in Fig. 1(A).

The relative densities of these three geometries are very close, specified as 9.0311% for Randomness I, 8.9199% for Randomness II, and 9.1022% for Randomness III. Fig. 8 presents the effects of random cell geometry on the stress-strain curves and energy absorption versus strain curves. It should be noted that the stress is calculated with the contact force and the strain is the nominal strain of porous structures. It can be seen that, although the stresses at the impact and stationary ends vary slightly with different geometries, the energy absorptions with Randomness I, II and III are almost identical during the whole crushing progress, indicating that the energy absorption capacity of porous structures is independent of the geometrical randomness.

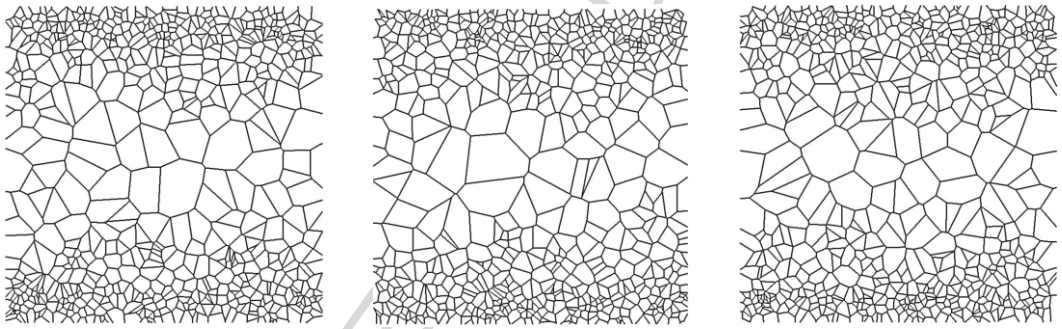

(A) Randomness I (B) Randomness II (C) Randomness III

Fig. 7. Different random cell geometries for non-uniform symmetric porosity distribution.

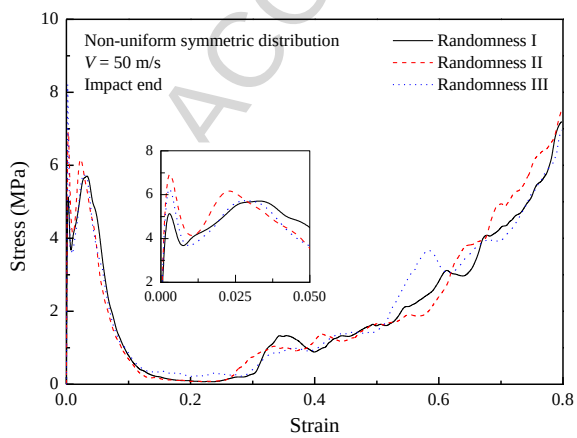

(A) Stress-strain curves at the impact end

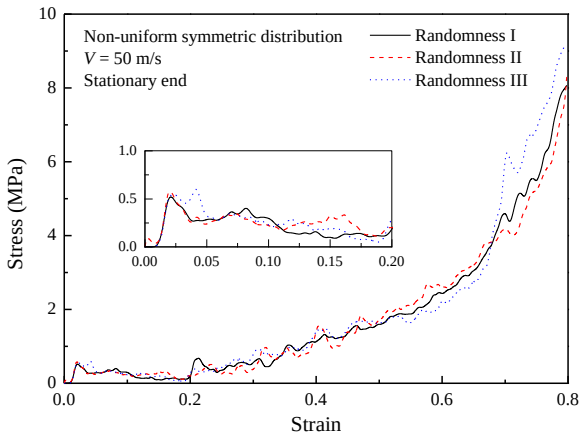

(B) Stress-strain curves at the stationary end

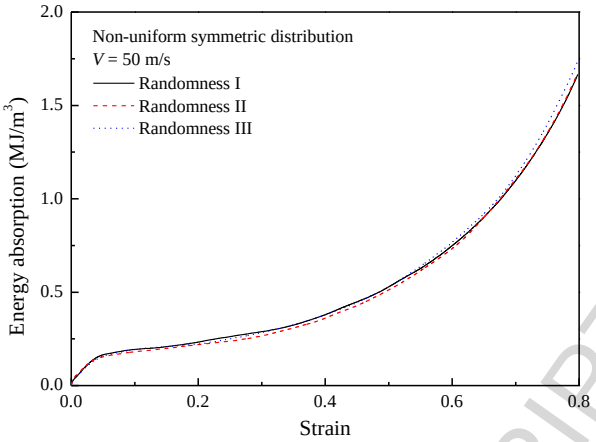

(C) Energy absorption versus strain curves

Fig. 8. Stress-strain curves and energy absorption versus strain curves of porous structures: effect of random cell geometry ($V = 50$ m/s).

3.4 Effect of porosity gradient

Different porosity gradients can be employed for the similar FG distribution, as shown in Fig. 9 with four different gradient patterns for non-uniform symmetric porosity. The average size of internal pores on the mid-plane is the largest for Gradient I and the smallest for Gradient IV. Thus, the variation of porosity is the most obvious for Gradient I and the least pronounced for Gradient IV. The corresponding variations of internal pore number $\mathrm{S}(z)$ are quantified by using Eq. (1) with the coefficients specified in Table 3. For Gradient IV, the porosity distribution cannot be described with polynomial curves as the pore number approximately equals to 20 along the horizontal direction around the mid-plane ($|z| < 0.015$ m), which increases and reaches over 45 near the surfaces ($|z| > 0.020$ m). For different patterns, the relative densities are similar, i.e., 9.0105% for Gradient I, 9.0311% for Gradient II, 9.0085% for Gradient III, and 9.0165% for Gradient IV. The stress-strain curves on the impact and stationary ends of porous structures with different porosity gradients are

illustrated in Fig. 10(A) and Fig. 10(B), respectively. Results show that the stresses on the stationary end are fairly close for all patterns with small vibrations due to the irregular porosity geometries, while that on the impact end varies more dramatically with Gradient I due to the larger pore size on the mid-plane. Fig. 10(C) gives the energy absorption versus strain curves for all patterns. It can been seen that when the impact velocity $V = 50$ m/s, the energy absorption capacity of FG porous structures is only slightly influenced by the porosity gradient.

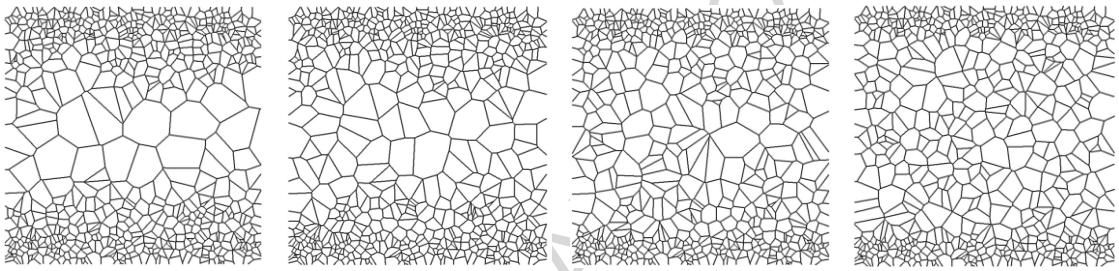

Gradient I Gradient II Gradient III Gradient IV

Fig. 9. Different porosity gradients for non-uniform symmetric porosity distribution.

Table 3

Coefficient in polynomials of internal pore numbers for porosities with different gradients.

Porosity distribution	S_1	S_2	S_3	S_4	z (m)
Gradient I	-4.1143e6	1.9019e5	-541.3039	9.7146	$0 < z < 0.025$
Gradient II	-2.9447e6	1.4895e5	-301.3133	11.2830	$0 < z < 0.025$
Gradient III	-7.3973e5	9.3790e4	-480.7264	16.4333	$0 < z < 0.025$

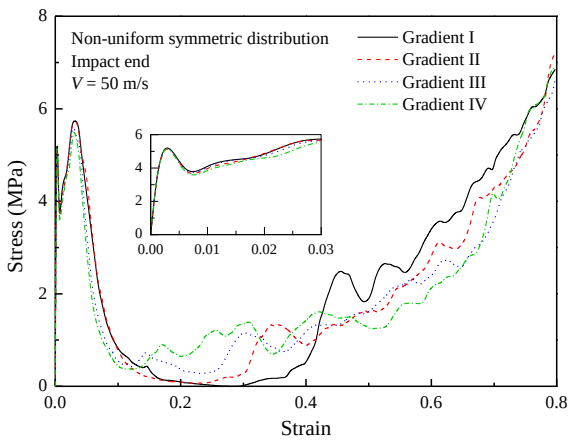

(A) Stress-strain curves at the impact end

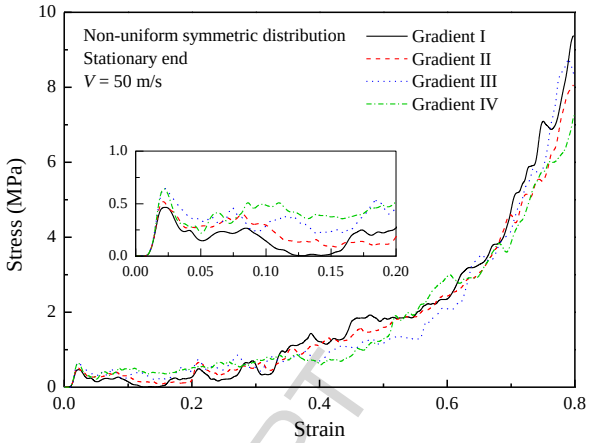

(B) Stress-strain curves at the stationary end

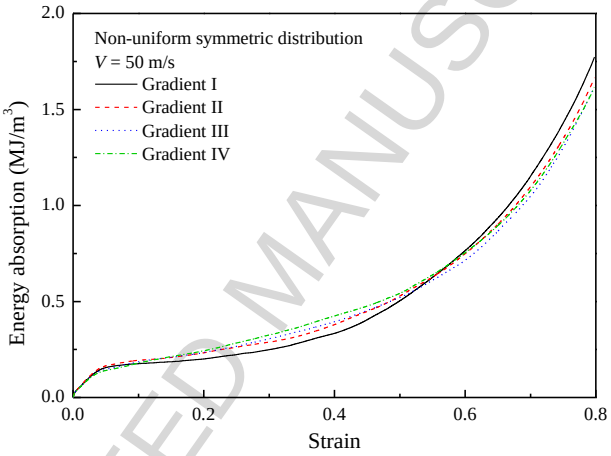

(C) Energy absorption versus strain curves

Fig. 10. Stress-strain curves and energy absorption versus strain curves of porous structures: effect of porosity gradient ($V = 50$ m/s).

3.5 Effect of cell wall thickness

The effect of cell wall thickness is examined based on the non-uniform distribution A with the porosity geometry given in Fig. 1(A). The relative density increases proportionally with the increasing of cell wall thickness, as given in Table 4. Fig. 11 presents the effects of cell wall thickness on the stress-strain and energy absorption curves. As expected, the increasing

of cell wall thickness leads to a sharp growth of contact stresses on both impact and stationary ends, as well as an evident increase in the energy absorption capacity of porous structures.

Table 4

Relative density of non-uniform distribution A with different cell wall thicknesses.

Cell wall thickness (mm)	Relative density (%)
0.05	4.5155
0.10	9.0311
0.15	13.547
0.20	18.062

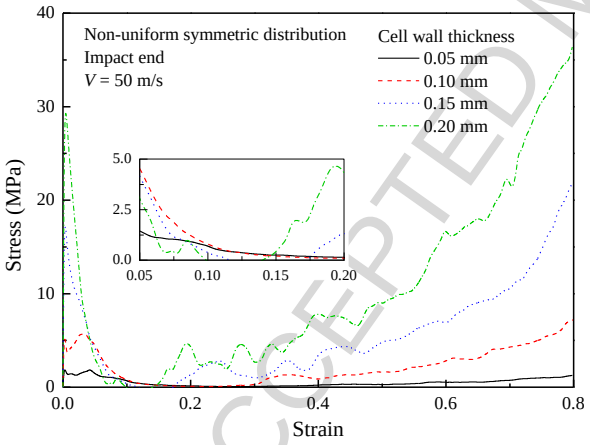

(A) Stress-strain curves at the impact end

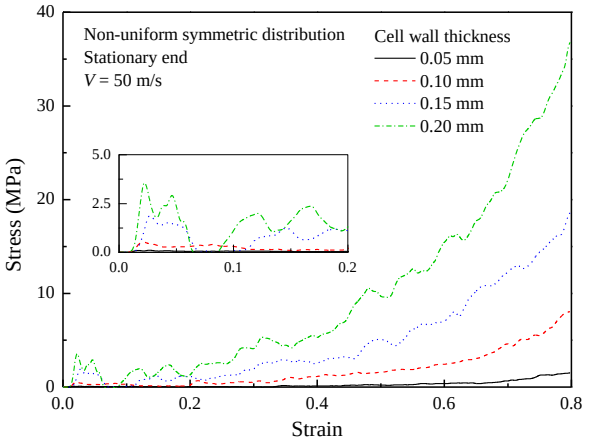

(B) Stress-strain curves at the stationary end

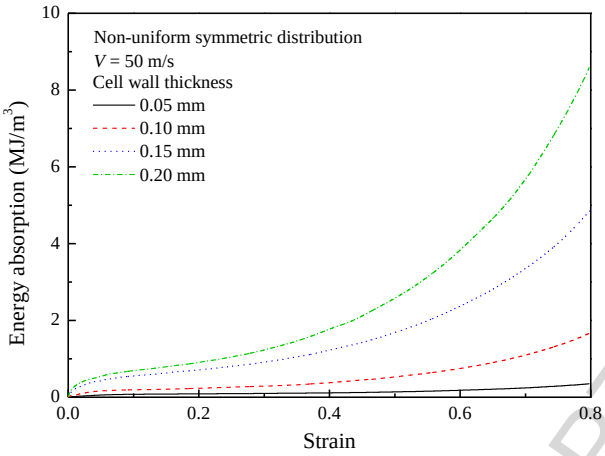

(C) Energy absorption versus strain curves

Fig. 11. Stress-strain curves and energy absorption versus strain curves of porous structures: effect of cell wall thickness ($V = 50$ m/s).

3.6 Effect of internal pore number

Fig. 12 shows four patterns of non-uniform symmetric porosity distribution with internal pore number $\mathrm{S}(z)$ decreasing from Number I to Number IV with coefficients given in Table 5, while the corresponding cell wall thickness increases simultaneously, leading to similar relative densities listed in Table 6. The effects of internal pore number on the stress-strain and energy absorption curves are presented in Fig. 13. It can be found that the overall contact stress variations on both ends for all patterns are quite close to each other, except for the beginning part on the impact end with much higher stresses for Number III and Number IV. The energy absorption of Number IV is the highest, indicating that under the same relative density, decreasing the internal pore number and increasing the cell wall thickness can enhance the energy absorption capacity of porous structures.

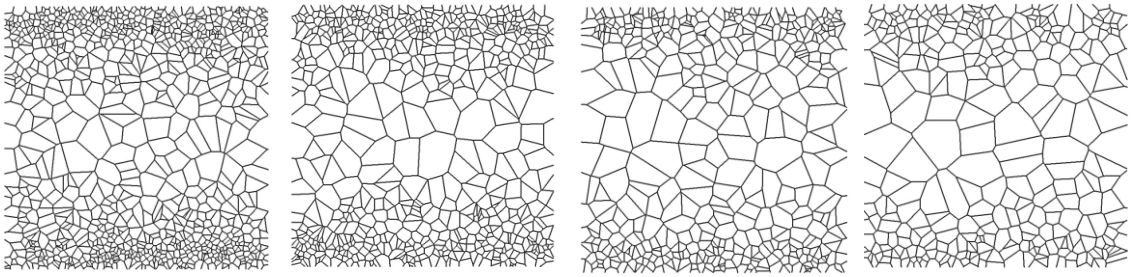

Number I Number II Number III Number IV

Fig. 12. Different internal pore numbers for non-uniform symmetric porosity distribution.

Table 5

Coefficient in polynomials of internal pore numbers for porosities with different pore numbers.

Porosity distribution	S_1	S_2	S_3	S_4	z (m)
Number I	-3.0639e6	1.8236e5	-862.8188	17.5934	$0 < z < 0.025$
Number II	-2.9447e6	1.4895e5	-301.3133	11.2830	$0 < z < 0.025$
Number III	-2.3350e6	1.3825e5	-925.3531	13.6733	$0 < z < 0.025$
Number IV	-7.0019e5	4.3797e4	425.4910	8.2093	$0 < z < 0.025$

Table 6

Relative density of non-uniform distribution A with different internal pore numbers.

Pattern	Cell wall thickness (mm)	Relative density (%)
Number I	0.08	8.9526
Number II	0.10	9.0311
Number III	0.12	8.9854
Number IV	0.14	8.9513

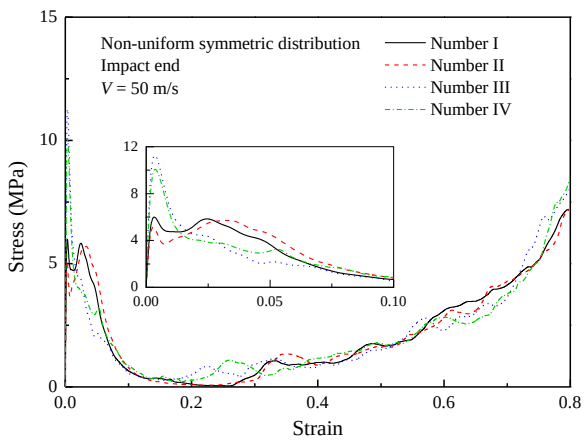

(A) Stress-strain curves at the impact end

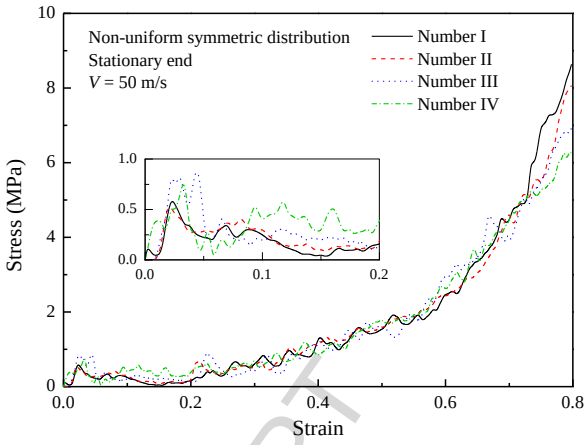

(B) Stress-strain curves at the stationary end

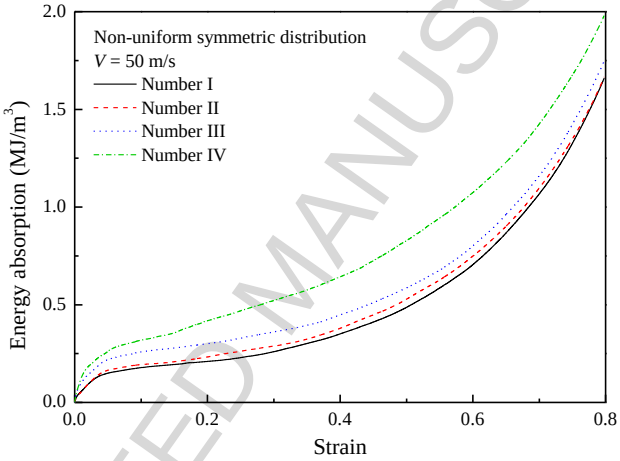

(C) Energy absorption versus strain curves

Fig. 13. Stress-strain curves and energy absorption versus strain curves of porous structures: effect of internal pore number ($V = 50$ m/s).

3.7 Effect of impact velocity

In this section, the effect of impact velocity is studied based on the patterns illustrated in Fig. 1 for different porosity distributions. Fig. 14 presents the effect of impact velocity on the stress-strain curves at the impact ends of porous structures with different porosity distributions. As can be seen, there is no obvious change of plateau stress and densification strain when the impact velocity is raised from 10 m/s to 50 m/s, indicating similar absorbed

energies. While in case of $V = 100$ or 200 m/s, the contact stress increases dramatically and varies based on different porosity distributions. Since the internal pores are generally crushed around the impact panel during high-velocity impacting as indicated by the deformation patterns in Fig. 19, larger value of stress at the impact end is induced by the crushing of internal pores with smaller size. The observed fluctuations are caused by the rapid compression of cell walls.

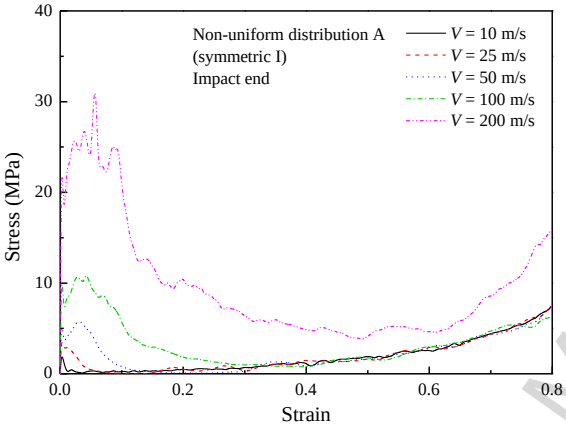

(A) Distribution A

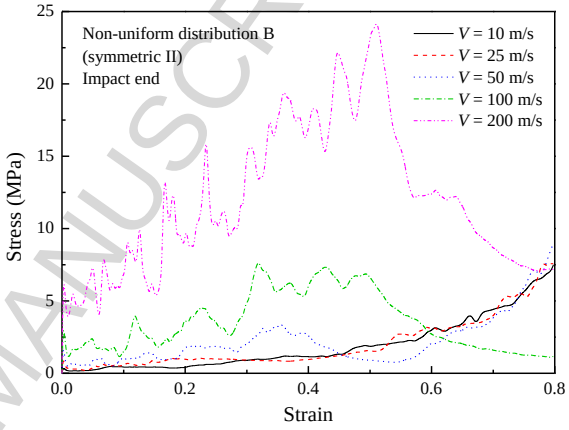

(B) Distribution B

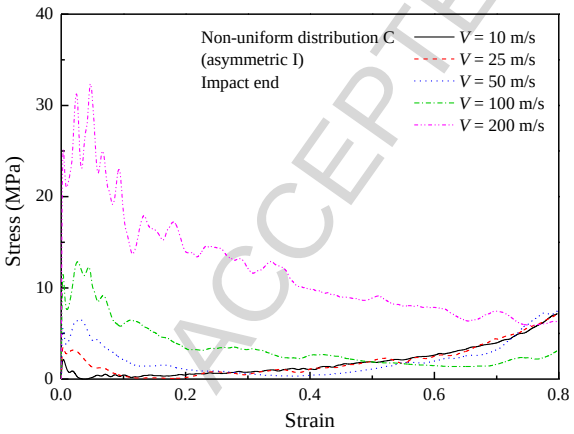

(C) Distribution C

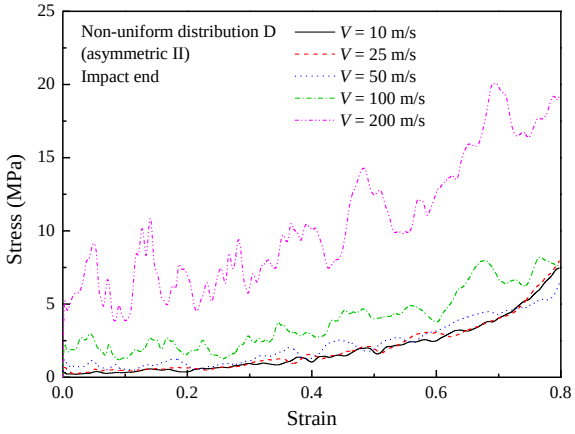

(D) Distribution D

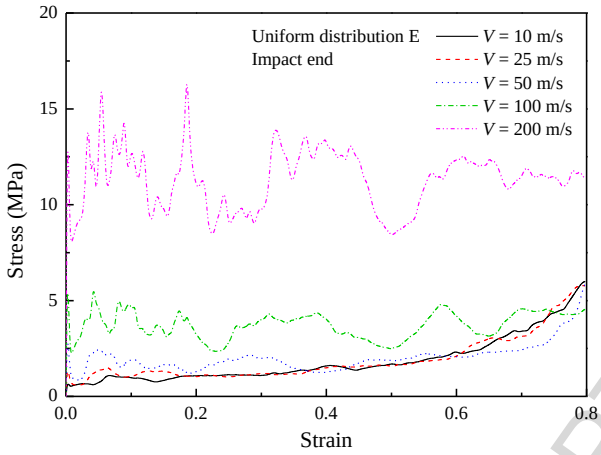

(E) Distribution E

Fig. 14. Stress-strain curves at the impact ends of porous structures with different porosity distributions: effect of impact velocity.

As showed in Fig. 15, the stress-strain curves at the stationary ends under low impact velocities ($V \leq 50$ m/s) are fairly close, suggesting that the impact wave has enough time to propagate from the top end to the bottom end, resulting in similar stress variations as that of quasi-static (QS) analysis. However, when $V = 100$ m/s, the impact wave can only arrive at the bottom end when the deformation is relatively large, as evidenced by the sharp rise at the end of stress-strain curves. Meanwhile, when $V = 200$ m/s, the impact wave cannot arrive at the bottom end during the simulation, leading to the small contact stress over the entire progress of crushing. According to Fig. 14 and Fig. 15, it can be found that the stress-strain curves of low velocity impacting ($V \leq 50$ m/s) at both impact and stationary ends are consistent with the QS compression curve, while those of high velocity impacting ($V = 100/200$ m/s) are related to the porosity distribution, as the deformation of porous structures is more localized around the impact panel with the increasing of the impact velocity.

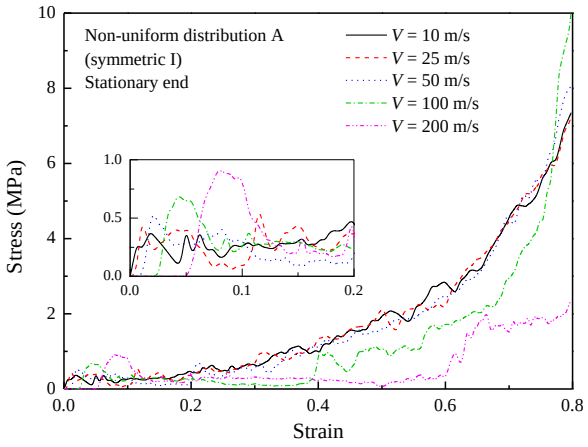

(A) Distribution A

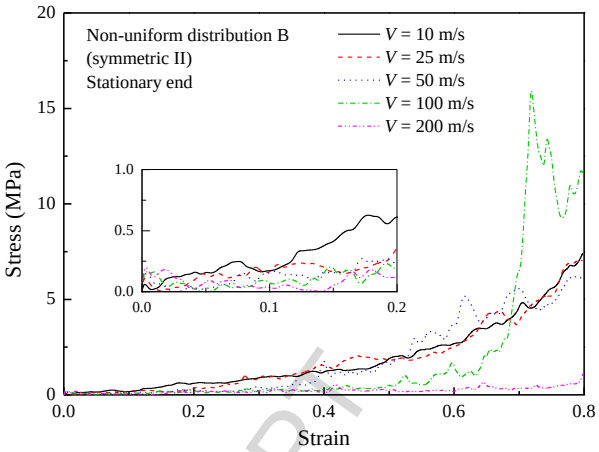

(B) Distribution B

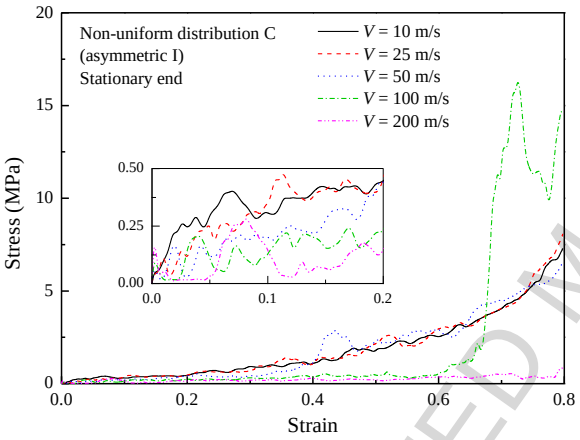

(C) Distribution C

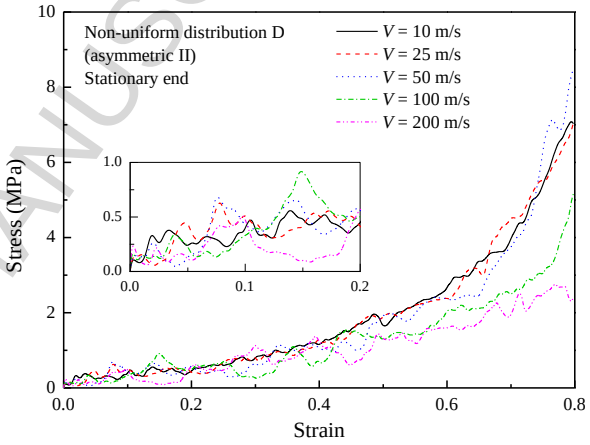

(D) Distribution D

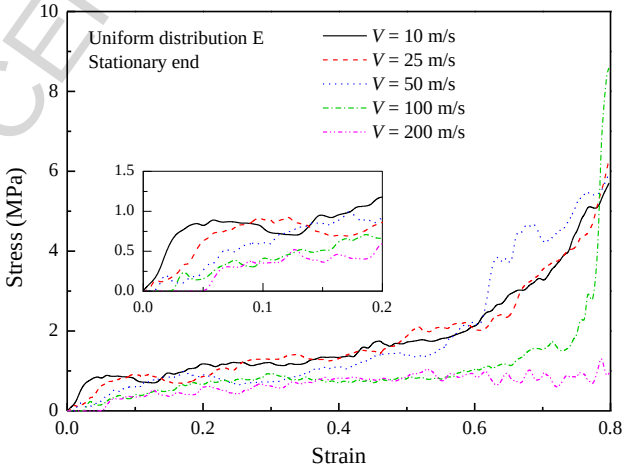

(E) Distribution E

Fig. 15. Stress-strain curves at the stationary ends of porous structures with different porosity distributions: effect of impact velocity.

Fig. 16 shows the effect of impact velocity on the energy absorption of porous structures with non-uniform distribution A. It can be seen that under the same strain, the absorbed energy remains almost the same when $V \leq 50$ m/s, while increases evidently when V is increased over 100 m/s. The results for other porosity distributions are quite similar and not given here for brevity.

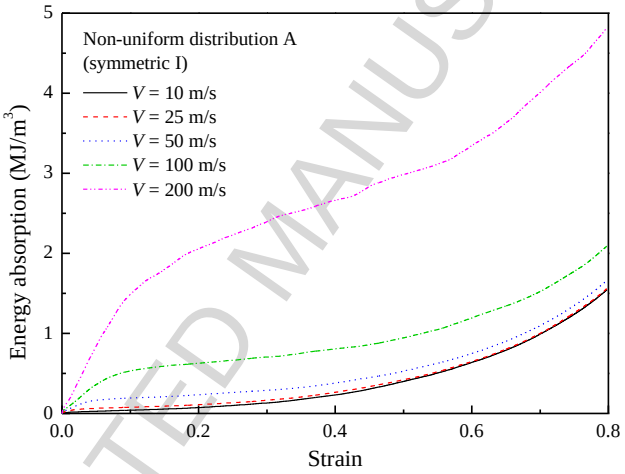

Fig. 16. Energy absorption versus strain curves of porous structures with non-uniform distribution A: effect of impact velocity.

Fig. 17 compares the energy absorption versus strain curves of porous structures and presents the difference induced by varying porosity distributions under different impact velocities. It is interesting to see that when $V = 10$ m/s, the energies absorbed by FG porosities A, B, C, and D are nearly the same during the crushing, while that absorbed by uniform porosity E is the largest. The difference between energy absorptions for uniform and non-uniform porosities increases in the beginning of crushing and drops by the end. It can

also be seen that under the low velocity impacting ($V \leq 50$ m/s), uniform porosity distribution E is preferred with the better energy absorption capacity.

However, as the impact velocity increases to 100 or 200 m/s, the energy absorption of asymmetric distribution C turns out to be the largest under the same strain, while that of asymmetric distribution D is the smallest. Therefore, smaller size and larger density of internal pores close to the impact end will significantly improve the energy absorption capacity of porous structures under a high-velocity impact. When the strain is maximized at 0.8 with the porous structure being highly densified, the absorbed energies for different porosities under the same impact velocity are nearly identical, as the similar relative densities are employed for all distributions.

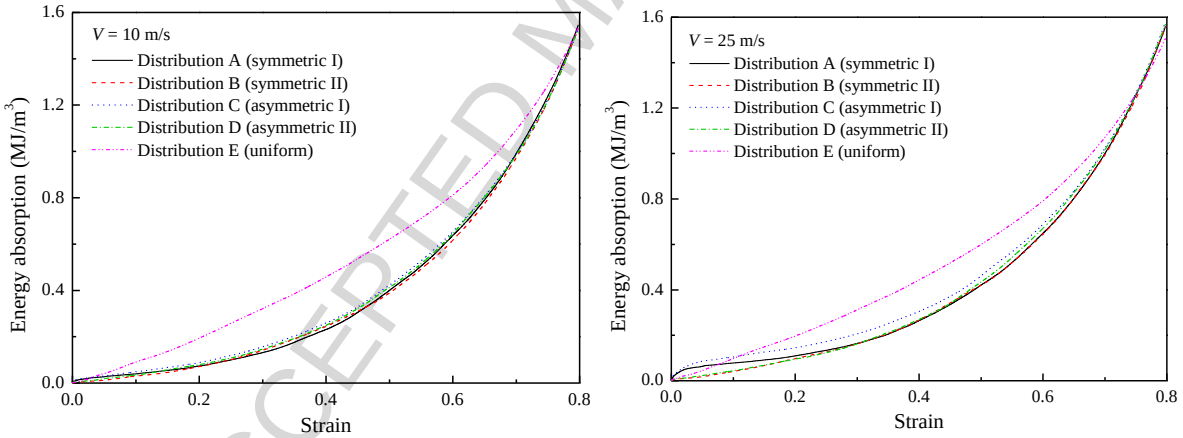

(A) V = 10 m/s (B) V = 25 m/s

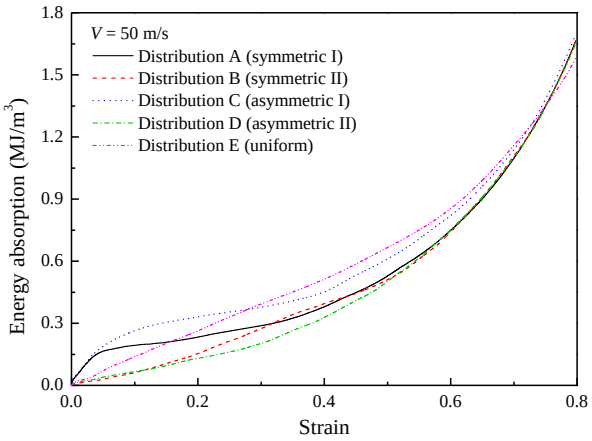

(C) V = 50 m/s

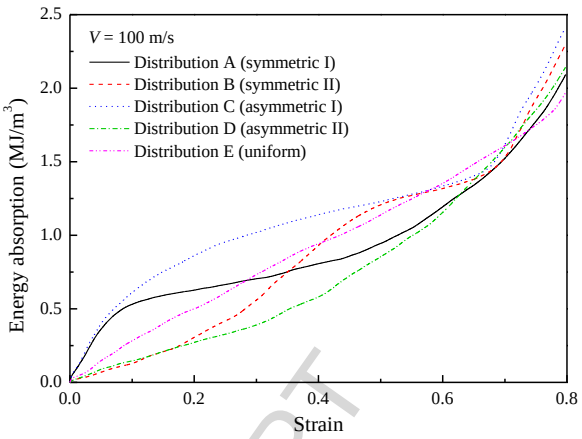

(D) V = 100 m/s

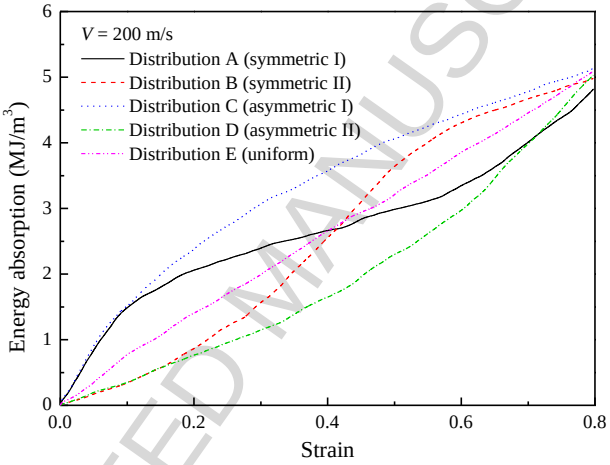

(E) V = 200 m/s

Fig. 17. Comparisons of energy absorption versus strain curves of porous structures with different porosity distributions.

Fig. 18 depicts the deformation patterns of porous structures with non-uniform distribution A and uniform distribution E when V = 50 m/s. Results show that the densification of non-uniform porosity is first localized in the weak part with large size of internal pores, resulting in the so-called deformation band. While for the uniform distribution, no deformation band is observed as the densification is quite evenly distributed.

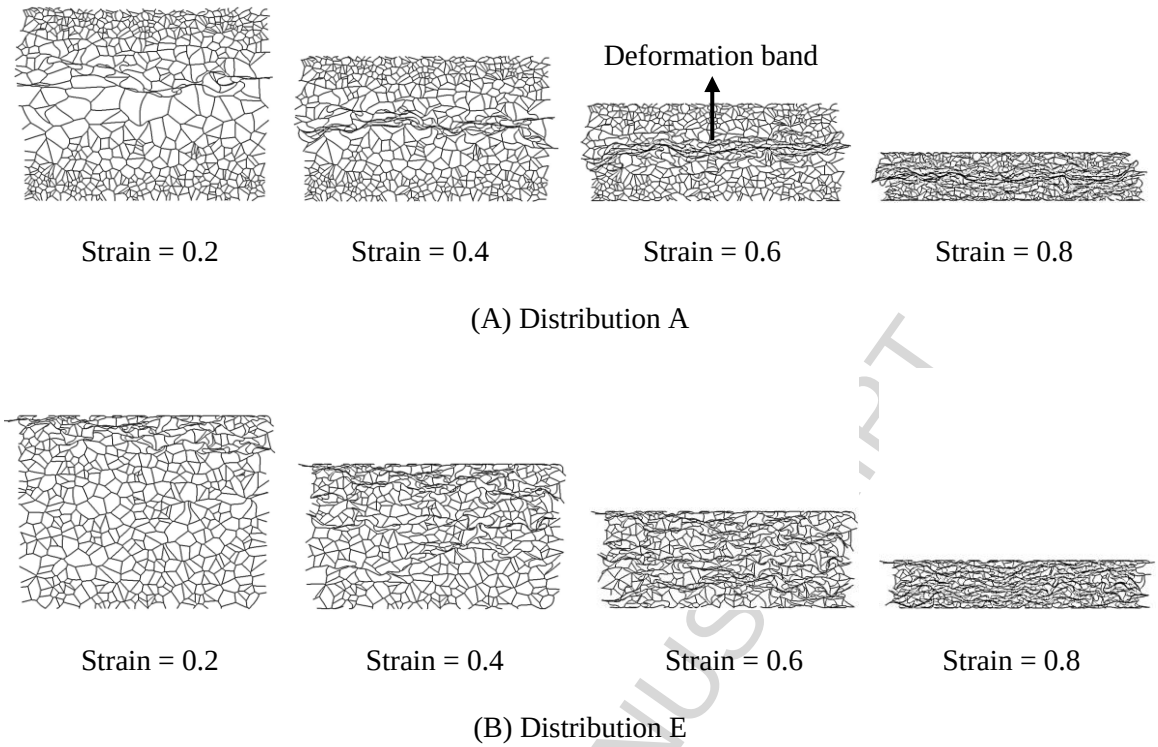

Fig. 18. Deformation patterns of porous structures with different porosity distributions (V = 50 m/s).

Fig. 19 presents the effect of high impact velocity on the deformation patterns of porous structures with non-uniform distribution A. It should be noted that there is no obvious change in the deformation pattern with low impact velocities ($V \leq 50$ m/s). Nevertheless, when the velocity increases to 100 or 200 m/s, the densification tends to localize near the impact end while the cell walls on the stationary end remain almost intact especially when V = 200 m/s, as the impact wave cannot propagate through the whole structure during the crushing progress under a high-velocity impact. It also can be observed that porous structures under high velocity impacting are more compressed and densified in the deformation area, leading to larger absorbed energies, as evidenced by the results given in Fig. 16.

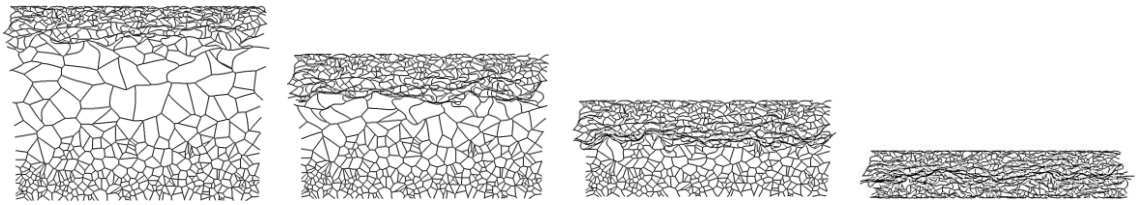

Strain = 0.2 Strain = 0.4 Strain = 0.6 Strain = 0.8

(A) $V = 100$ m/s

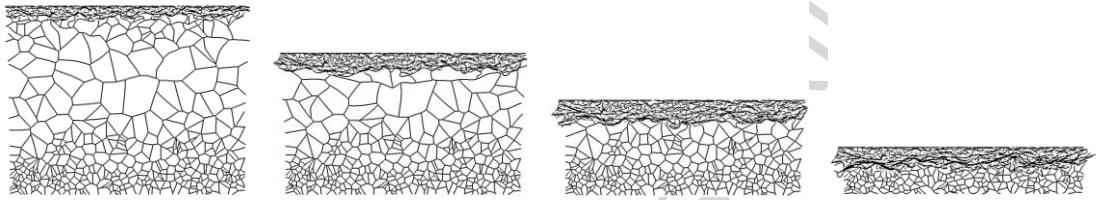

Strain = 0.2 Strain = 0.4 Strain = 0.6 Strain = 0.8

(B) $V = 200$ m/s

Fig. 19. Deformation patterns of porous structures with non-uniform distribution A: effect of high impact velocity.

4. Conclusions

This paper presents an explicit dynamic analysis of FG porous structures under varying impact velocities. The effects of random cell geometry, porosity gradient, cell wall thickness, internal pore number, and impact velocity on the energy absorption, deformation pattern, and stress-strain curves on both impact and stationary ends are investigated and discussed in detail. Based on the numerical results, the following conclusions can be obtained.

(1) When the impact velocity $V = 50$ m/s, the geometrical randomness and porosity gradient have no evident influence on the energy absorption of FG porous structures, which can be remarkably raised by increasing the cell wall thickness under the same porosity geometry.

(2) Decreasing the internal pore number and increasing the cell wall thickness can improve the energy absorption capacity of FG porous structures with the same relative density.

(3) The variation of contact stress follows the typical QS compression curve with low impact velocities ($V \leq 50$ m/s), while depends on the distribution of internal pores under a high velocity impact ($V = 100$ or 200 m/s).

(4) The absorbed energy of porous structures increases with the increasing of impact velocity.

(5) Under low impact velocities, the energy absorption capacity of porous structures with uniform distribution E is the best, while the FG porous structure with non-uniformly asymmetric distribution C is preferred under a high-velocity impact. Thus, the porosity distribution of porous structures can be designed as uniform or non-uniform to improve the energy absorption capacity under different impact velocities.

(6) The deformation pattern of FG porous structures is dependent on the porosity distribution. And the densification during the crushing progress tends to localize near the impact end under high impact velocities.

The findings are based on the 2D assumptions and the constant-velocity crushing. All the corresponding issues have been discussed in detail, as well as the reason for the limited validation. With all these drawbacks, we still believe in the reliability of the findings, as the proposed numerical modelling is suitable for this study and sufficient to obtain reasonable results. The results are interesting and provide useful advice for the porosity design regarding the dynamic crushing. By simply changing the distribution patterns of internal pores, we can actually enhance the energy absorption capacities of metal foams, which is very exciting. Our research can be further improved by adopting both 3D modelling and 3D printing to fully reveal the novel structural properties of functionally graded metal foams. Since as mentioned,

the perfect match between the numerical modelling and experiments can only be achieved by building the models based on the SEM imaging or manufacturing the specimens with 3D printing. The latter method is preferred as the imperfections within the traditional manufacture progress can be avoided. Especially for the presented study, functionally graded porosities cannot be easily obtained with the traditional manufacture techniques. Meanwhile, 3D printing is an effective method to construct the desired non-uniform porosity geometries with selective laser melting (SLM) for open-cell metal foams. While for closed-cell metal foams, other methods need to be proposed as the extra metallic powders in SLM cannot be taken out from the closed cells. All of these are included in our research plan.

Acknowledgements

The work described in this paper was fully funded by an Australian Government Research Training Program Scholarship and three research grants from the Australian Research Council under Discovery Project scheme (DP160101978) and Linkage Project scheme (LP150100103, LP150101033). The authors are grateful for their financial support.

References

[1] L. J. Gibson, M. F. Ashby, Cellular solids: Structure and properties, Cambridge University Press, Cambridge, UK, 1997.

[2] M. F. Ashby, T. Evans, N. A. Fleck, J. Hutchinson, H. Wadley, L. Gibson, Metal foams: A design guide, Butterworth-Heinemann, Boston, USA, 2000.

[3] B. Smith, S. Szyniszewski, J. Hajjar, B. Schafer, S. Arwade, Steel foam for structures: A review of applications, manufacturing and material properties, Journal of Constructional Steel Research 71 (2012) 1-10.

[4] J. Banhart, Manufacture, characterisation and application of cellular metals and metal foams, Progress in Materials Science 46 (2001) 559-632.

[5] C. Betts, Benefits of metal foams and developments in modelling techniques to assess their materials behaviour: A review, Materials Science and Technology 28 (2012) 129-143.

[6] J. Hohe, V. Hardenacke, V. Fascio, Y. Girard, J. Baumeister, K. Stöbener, J. Weise, D. Lehmhus, S. Pattofatto, H. Zeng, Numerical and experimental design of graded cellular sandwich cores for multi-functional aerospace applications, Materials & Design 39 (2012) 20-32.

[7] N. Dukhan, Metal foams: Fundamentals and applications, DEStech Publications, Inc, Lancaster, USA, 2013.

[8] L. P. Lefebvre, J. Banhart, D. Dunand, Porous metals and metallic foams: Current status and recent developments, Advanced Engineering Materials 10 (2008) 775-787.

[9] C. Zhao, Review on thermal transport in high porosity cellular metal foams with open cells, International Journal of Heat and Mass Transfer 55 (2012) 3618-3632.

[10] G. Davies, S. Zhen, Metallic foams: Their production, properties and applications, Journal of Materials Science 18 (1983) 1899-1911.

[11] A. Rabiei, L. Vendra, A comparison of composite metal foam's properties and other comparable metal foams, Materials Letters 63 (2009) 533-536.

[12] A. Wiest, C. A. MacDougall, R. D. Conner, Optimization of cellular solids for energy absorption, Scripta Materialia 84 (2014) 7-10.

[13] F. Yi, Z. Zhu, F. Zu, S. Hu, P. Yi, Strain rate effects on the compressive property and the energy-absorbing capacity of aluminum alloy foams, Materials Characterization 47 (2001) 417-422.

[14] A. Jung, H. Natter, S. Diebels, E. Lach, R. Hempelmann, Nanonickel coated aluminum foam for enhanced impact energy absorption, Advanced Engineering Materials 13 (2011) 23-28.

[15] M. Idris, T. Vodenitcharova, M. Hoffman, Mechanical behaviour and energy absorption of closed-cell aluminium foam panels in uniaxial compression, Materials Science and Engineering: A 517 (2009) 37-45.

[16] Z. Zheng, J. Yu, C. Wang, S. Liao, Y. Liu, Dynamic crushing of cellular materials: A unified framework of plastic shock wave models, International Journal of Impact Engineering 53 (2013) 29-43.

[17] C. G. Aneziris, H. Berek, M. Hasterok, H. Biermann, S. Wolf, L. Krüger, Novel trip-steel/mg-psz composite–open cell foam structures for energy absorption, Advanced Engineering Materials 12 (2010) 197-204.

[18] B. Koohbor, A. Kidane, Design optimization of continuously and discretely graded foam materials for efficient energy absorption, Materials & Design 102 (2016) 151-161.

[19] Z. Zheng, C. Wang, J. Yu, S. R. Reid, J. J. Harrigan, Dynamic stress–strain states for metal foams using a 3d cellular model, Journal of the Mechanics and Physics of Solids 72 (2014) 93-114.

[20] M. Kader, M. Islam, P. Hazell, J. Escobedo, M. Saadatfar, A. Brown, G. Appleby-Thomas, Modelling and characterization of cell collapse in aluminium foams during dynamic loading, International Journal of Impact Engineering 96 (2016) 78-88.

[21] D. Li, L. Dong, J. Yin, R. S. Lakes, Negative poisson's ratio in 2d voronoi cellular solids by biaxial compression: A numerical study, Journal of Materials Science 51 (2016) 7029-7037.

[22] Q. Fang, J. Zhang, Y. Zhang, J. Liu, Z. Gong, Mesoscopic investigation of closed-cell aluminum foams on energy absorption capability under impact, Composite Structures 124 (2015) 409-420.

[23] M. Vesenjak, C. Veyhl, T. Fiedler, Analysis of anisotropy and strain rate sensitivity of open-cell metal foam, Materials Science and Engineering: A 541 (2012) 105-109.

[24] D. Chen, J. Yang, S. Kitipornchai, Elastic buckling and static bending of shear deformable functionally graded porous beam, Composite Structures 133 (2015) 54-61.

[25] D. Chen, J. Yang, S. Kitipornchai, Free and forced vibrations of shear deformable functionally graded porous beams, International Journal of Mechanical Sciences 108 (2016) 14-22.

[26] D. Chen, S. Kitipornchai, J. Yang, Nonlinear free vibration of shear deformable sandwich beam with a functionally graded porous core, Thin-Walled Structures 107 (2016) 39-48.

[27] S. Kitipornchai, D. Chen, J. Yang, Free vibration and elastic buckling of functionally graded porous beams reinforced by graphene platelets, Materials & Design 116 (2017) 656-665.

[28] D. Chen, J. Yang, S. Kitipornchai, Nonlinear vibration and postbuckling of functionally graded graphene reinforced porous nanocomposite beams, Composites Science and Technology 142 (2017) 235-245.

[29] E. Magnucka-Blandzi, Dynamic stability of a metal foam circular plate, Journal of Theoretical and Applied Mechanics 47 (2009) 421-433.

[30] A. Mojahedin, M. Jabbari, A. Khorshidvand, M. Eslami, Buckling analysis of functionally graded circular plates made of saturated porous materials based on higher order shear deformation theory, Thin-Walled Structures 99 (2016) 83-90.

[31] A. Ajdari, H. Nayeb-Hashemi, A. Vaziri, Dynamic crushing and energy absorption of regular, irregular and functionally graded cellular structures, International Journal of Solids and Structures 48 (2011) 506-516.

[32] M. Liang, Z. Li, F. Lu, X. Li, Theoretical and numerical investigation of blast responses of continuous-density graded cellular materials, Composite Structures 164 (2017) 170-179.

[33] A. Okabe, B. Boots, K. Sugihara, S. N. Chiu, Spatial tessellations: Concepts and applications of voronoi diagrams, Vol. 501. Published, John Wiley & Sons, 2009.

[34] Y. H. Lu, Integration of rp and explicit dynamic fem for the visualization of the sheet metal forming process, The International Journal of Advanced Manufacturing Technology 28 (2006) 255-261.

[35] Ls-dyna keyword user's manual (version 971), Livermore Software Technology Corporation, Livermore, CA, USA, 2007.

[36] L. Jing, Z. Wang, L. Zhao, Dynamic response of cylindrical sandwich shells with metallic foam cores under blast loading — numerical simulations, Composite Structures 99 (2013) 213-223.

[37] P. Tan, S. Reid, J. Harrigan, Z. Zou, S. Li, Dynamic compressive strength properties of aluminium foams. Part i — experimental data and observations, Journal of the Mechanics and Physics of Solids 53 (2005) 2174-2205.

[38] I. Duarte, M. Vesenjak, L. Krstulović-Opara, Variation of quasi-static and dynamic compressive properties in a single aluminium foam block, Materials Science and Engineering: A 616 (2014) 171-182.

[39] K. A. Dannemann, J. Lankford, High strain rate compression of closed-cell aluminium foams, Materials Science and Engineering: A 293 (2000) 157-164.

[40] J. Zhang, Z. Wang, L. Zhao, Dynamic response of functionally graded cellular materials based on the voronoi model, Composites Part B: Engineering 85 (2016) 176-187.

[41] G. Ma, Z. Ye, Z. Shao, Modeling loading rate effect on crushing stress of metallic cellular materials, International Journal of Impact Engineering 36 (2009) 775-782.

[42] E. Q. Sun. Shear locking and hourglassing in msc nastran, abaqus, and ansys. In: Msc software users meeting. 2006.

[43] I. Irausquín, J. Pérez-Castellanos, V. Miranda, F. Teixeira-Dias, Evaluation of the effect of the strain rate on the compressive response of a closed-cell aluminium foam using the split hopkinson pressure bar test, Materials & Design 47 (2013) 698-705.

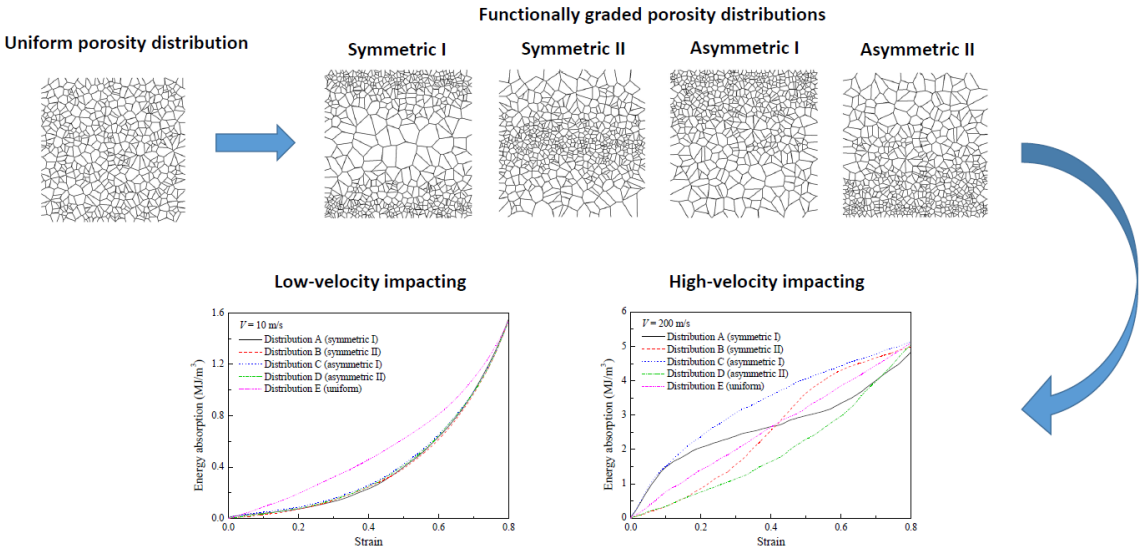

Graphical abstract

Highlights:

- The porosity distribution of porous structures has a significant influence on the dynamic response.
- The energy absorption under high-velocity impacting can be considerably improved with the proposed graded porosity distribution.
- The absorbed energy of porous structures increases with the increasing impact velocity.
- The densification of cell walls tends to localize near the impact end under high impact velocities.